Enhanced magnetic anisotropy induced by praseodymium ferromagnetic order and anomalous transport properties in $PrMn_2Ge_2$ single crystals

Dan Huang,[1] Hang Li,[1,2] Bei Ding,[1] Xuekui Xi,[1,*] Yong-Chang Lau,[1,3] and Wenhong Wang[2,†]

[1]*Beijing National Laboratory for Condensed Matter Physics, Institute of Physics, Chinese Academy of Sciences, Beijing 100190, China*

[2]*School of Electronic and Information Engineering, Tiangong University, Tianjin 300387, China*

[3]*University of Chinese Academy of Sciences, Beijing 100049, China*

(Received 22 March 2023; revised 3 June 2023; accepted 5 June 2023; published 16 June 2023)

Anisotropic magnetization and anomalous electrical transport properties of flux-grown $PrMn_2Ge_2$ single crystals were investigated. The grown crystals exhibit strong magnetic anisotropy with easy magnetization along the *c* axis. Linear magnetoresistance (MR) and a conventional anomalous Hall effect (AHE) are observed for *H*//*c* and *I*//*b* in contrast to a nonlinear positive MR and a large planar topological Hall effect (PTHE) observed for *H*//*a* and *I*//*b*. The anisotropy of the magnetic and electrical transport properties is increased as temperature decreases because magnetic ordering of Pr atoms brings about an increase of the saturation magnetic field of nonlinear MR and the critical field for the maximum values of PTHE. A scaling analysis using the Tian-Ye-Jin model suggests that the AHE in this compound has a larger intrinsic contribution compared to the extrinsic contribution. The nonlinear positive MRs are attributed to the field-induced nontrivial spin textures. The PTHE is related to the real-space skyrmionic bubbles and the noncoplanar spin texture with nonzero spin chirality. These results demonstrate a magnetic field induced anisotropic magnetoresistance and Hall resistivity and its tunability by the ferromagnetic ordering of rare earth atoms in conical-ordered magnets.

DOI: 10.1103/PhysRevB.107.224417

I. INTRODUCTION

The ternary intermetallic compounds RMn_2Ge_2 (R = rare earth) have been extensively studied with respect to various magnetic ordering and giant magnetocaloric effect near the magnetic transition temperature [1,2]. The magnetic structures and magnetic phase transitions of RMn_2Ge_2 can be tuned by the substitution of different rare earth atoms. Recently, the RMn_2Ge_2 compounds have attracted broad interest following the discovery of room-temperature magnetic skyrmions [3,4], which are topologically nontrivial spin textures. The special spin configurations can induce unusual magnetic and electrical transports such as the topological Hall effect (THE) and nonlinear magnetoresistance (MR) [5]. A large anomalous Hall effect (AHE) and THE have been observed in $LaMn_2Ge_2$ [6] and $CeMn_2Ge_2$ [7] and are related to the momentum-space and real-space Berry phases of conduction electrons, respectively [8]. Their magnitudes are sensitive to the details of the electronic and magnetic structures. The AHE is proportional to the spontaneous magnetization and it is usually interpreted by considering three mechanisms, i.e., skew scattering, side jump, and Berry curvature [8,9]. On the other hand, a THE is induced by the noncoplanar spin configuration or the topological windings of spin texture, known as skyrmions [10,11]. The AHE and THE of $CeMn_2Ge_2$ also show a significant anisotropy. The anisotropy is related to the magnetocrystalline anisotropy of the conical magnetic moment of the Mn atom because the Ce sublattice is not ordered at low temperatures [7,12]. Rare earth atoms have a strong single-ion anisotropy [13,14], and there exists a strong interaction between $3d$ electrons of Mn atoms and $4f$ electrons of rare earth atoms [15], which should affect the magnetoelectric transport properties of RMn_2Ge_2. Therefore, one of the aims of this paper is to study the effect of the magnetic moment of rare earth ions on the anisotropy of the magnetoelectric transport.

In the family of RMn_2Ge_2 compounds, $PrMn_2Ge_2$ is an ideal one to study the effect of rare earth ion anisotropy on magnetoelectric transport, because the type of the magnetic structure of Mn atoms in $PrMn_2Ge_2$ remains constant throughout the long-range magnetic ordering of rare earth atoms. At temperatures above T_C, the Mn sublattice of $PrMn_2Ge_2$ has a collinear antiferromagnetic structure in which the magnetic moment is perpendicular to the *c* axis. Below T_C these compounds have a canted spin structure, with a ferromagnetic component along the *c* axis. As the temperature goes below 280 K, the magnetic structure transforms from a canted to a conical ferromagnetic configuration. The magnetic structure of the Mn sublattice remains conical below this temperature [12,16,17]. The Pr sublattice becomes ferromagnetically ordered with moments parallel to the *c* axis when temperature is further decreased to 100 K [12]. A recent study of the anisotropic magnetic properties and critical behavior revealed that the magnetism of $PrMn_2Ge_2$ is dominated by the competition of long-range Ruderman-Kittel-Kasuya-Yosida (RKKY) and short-range exchange magnetic interactions [18]. Until now, the transport properties of $PrMn_2Ge_2$ have not been thoroughly investigated. On the other hand, a

*xi@iphy.ac.cn

†wenhongwang@tiangong.edu.cn

theoretical study predicted that the conical spin spiral texture can naturally produce a planar topological Hall effect (PTHE) when an external magnetic field is applied in the plane of the charge current [19]. It is well known that the planar Hall effect (PHE) refers to transverse Hall voltage induced by the coplanar electric and magnetic fields [20,21], which is essentially different from the usual Hall effect where they are mutually perpendicular to each other. The PTHE resembles a topological signal superimposed on the Hall resistivity with coplanar magnetic field and charge current, which has very recently been observed in skyrmion-hosting materials [22–24]. Following the above theoretical prediction and experimental studies, it is of fundamental interest to explore the magnetic and electric transport properties in the conical itinerant magnet $PrMn_2Ge_2$. In this paper, we report a study of the anisotropic magnetization behavior, magnetoresistance, and AHE of $PrMn_2Ge_2$ with the magnetic field in plane and out of plane. The results reveal a nonlinear magnetoresistance and PTHE in an in-plane magnetic field and the enhancement of the anisotropy of the magnetic and electric transport properties by the magnetic ordering of Pr atoms at low temperatures.

II. EXPERIMENTAL DETAILS

Single crystals of $PrMn_2Ge_2$ were grown in an indium flux. High-purity elemental Pr (99.9%), Mn (99.95%), Ge (99.999%), and In (99.99%) were mixed with a 1:2:2:20 molar ratio in an alumina crucible. The crucible was sealed in an evacuated quartz tube. The quartz tube was heated to 1423 K, soaked at this temperature for 24 h, and then cooled slowly to 973 K at a rate of 3 K/h. At this temperature, the excess indium was decanted using a centrifuge. Lamellar single crystals were the preferred growth. The as-grown crystals were characterized by the powder x-ray diffraction (XRD) technique in a PANalytical Empyrean with Cu $K\alpha$ radiation. The bulk composition of as-grown crystals was examined by energy-dispersive spectroscopy (EDS) in a Hitachi SU5000 scanning electron microscope (SEM). The atomic ratio of Pr:Mn:Ge determined by EDS is very close to the stoichiometry of 1:2:2 (Fig. S1 in the Supplemental Material [25]). The atomic-scale microstructure of crystals was investigated using a JEOL ARM200F scanning transmission electron microscope (STEM). Thermomagnetic and isothermal measurements were conducted on small pieces of a single crystal using a vibrating sample magnetometer attached to a Quantum Design superconducting quantum interference device (SQUID) in dc magnetic fields up to $\mu_0 H = 5$ T. The magnetoresistance (MR) and Hall resistivity of the samples at room and cryogenic temperatures in magnetic fields up to $\mu_0 H = 5$ T were measured using a Cryogenic Limited physical property measuring system (PPMS). A standard six-probe method was used to perform the resistivity and Hall resistivity measurements [22]. In these measurements, the samples were cut into a regular rectangular shape with a thickness of about 100 μm. The resistivity of the sample was determined using $\rho_{xx}(\mu_0 H) = [\rho_{xx}(+\mu_0 H) + \rho_{xx}(-\mu_0 H)]/2$ to reduce errors due to voltage probe misalignment. Correspondingly, the Hall resistivity of the sample was obtained using the equation $\rho_{xy}(\mu_0 H) = [\rho_{xy}(+\mu_0 H) - \rho_{xy}(-\mu_0 H)]/2$. The MR of the sample was defined as $[\rho_{xx}(H) - \rho_{xx}(0)]/\rho_{xx}(0)$, where $\rho_{xx}(H)$ and $\rho_{xx}(0)$ are the resistivities with and without a magnetic field, respectively. To study the anisotropy of the transverse magnetoresistance and the Hall effect, the magnetic field was applied out of plane ($H//c$) and in plane ($H//a$), respectively, and always perpendicular to the electrical current direction ($I//b$) [see the insets of Figs. 3(a) and 3(b)].

III. RESULTS AND DISCUSSION

$PrMn_2Ge_2$ crystallizes into a $ThCr_2Si_2$-type tetragonal structure with the space group $I4/mmm$. As shown in Fig. 1(a), the Pr, Mn, and Ge atoms are stacked in the layered sequence $\cdots \mathrm{Pr} - \mathrm{Ge} - \mathrm{Mn} - \mathrm{Ge} - \mathrm{Pr} \cdots$ along the c axis. The Mn atoms within the ab plane constitute a square lattice [Fig. 1(b)]. The nearest Mn-Mn intralayer distance given by $a/\sqrt{2}$ is smaller than that of interlayer separation $c/2$ [1]. Figure 1(c) shows the XRD pattern of a $PrMn_2Ge_2$ single crystal. Only $(00l)$ Bragg peaks are detected, indicating that the rectangular crystal surface is the ab plane. A typical crystal size of a single crystal piece is about $2 \times 2 \times 0.2\,\mathrm{mm}^3$ as presented in the inset of Fig. 1(c). A high-resolution STEM micrograph is shown in Fig. 1(d) and it confirms the high quality of the grown single crystals. Figure 1(e) shows the zero field cooling (ZFC) and field cooling (FC) curves of a $PrMn_2Ge_2$ single crystal in a magnetic field of $\mu_0 H = 0.01$ T applied along the a axis and c axis, respectively. The curves of the $PrMn_2Ge_2$ single crystal show three magnetic transitions on decreasing temperature: a ferromagnetic ordering of Mn, canted to conical ferromagnetic ordering of Mn (kinks in the dotted box), and ferromagnetic ordering of Pr. These transitions are consistent with those observed for $PrMn_2Ge_2$ polycrystals [16,17]. In Fig. 1(e), the starting and ending temperatures of ferromagnetic ordering of Pr are labeled as T_{C1}^{Pr} and T_{C2}^{Pr}, respectively. This is almost in agreement with the result of neutron diffraction as Pr establishes a magnetic moment of $1\mu_B$ and $2.95\,\mu_B$ at 142 and 2 K, respectively [12]. As shown in Fig. 1(e), the temperature dependence of magnetization curves is bifurcated at low temperatures for $H//a$ and $H//c$, indicating a significant magnetocrystalline anisotropy in this compound. When $H//a$, a drop of magnetization is observed in a low-temperature region. The drop is similar to that observed for a cooling-induced ferromagnetic to antiferromagnetic transition. An increase in magnetization is observed at the same temperature when $H//c$. The thermomagnetic curve shows an increase of the magnetization with the decreasing temperature due to the ordering of Pr magnetic moment around $T_{C1}^{\mathrm{Pr}} = 160$ K. It was suggested that the decrease of magnetization at $H//a$ is caused by the antiferromagnetically coupling of Pr and Mn at low temperature [18]. This seems to contradict the ferromagnetic coupling of Pr and Mn with $H//c$. The thermomagnetic and magnetoelectric transport measurements later allow us to conclude that there are ferromagnetic interactions between Pr and Mn, no matter whether a magnetic field is applied in the in-plane or out of plane directions. The decrease of magnetization in the $H//a$ at low temperatures is attributed to the enhanced magnetic anisotropy due to the magnetic ordering of Pr magnetic moments.

Figure 1(f) shows the resistivity $\rho_{xx}(T)$ of $PrMn_2Ge_2$ under zero field in the temperature range $4 - 380$ K indicating a

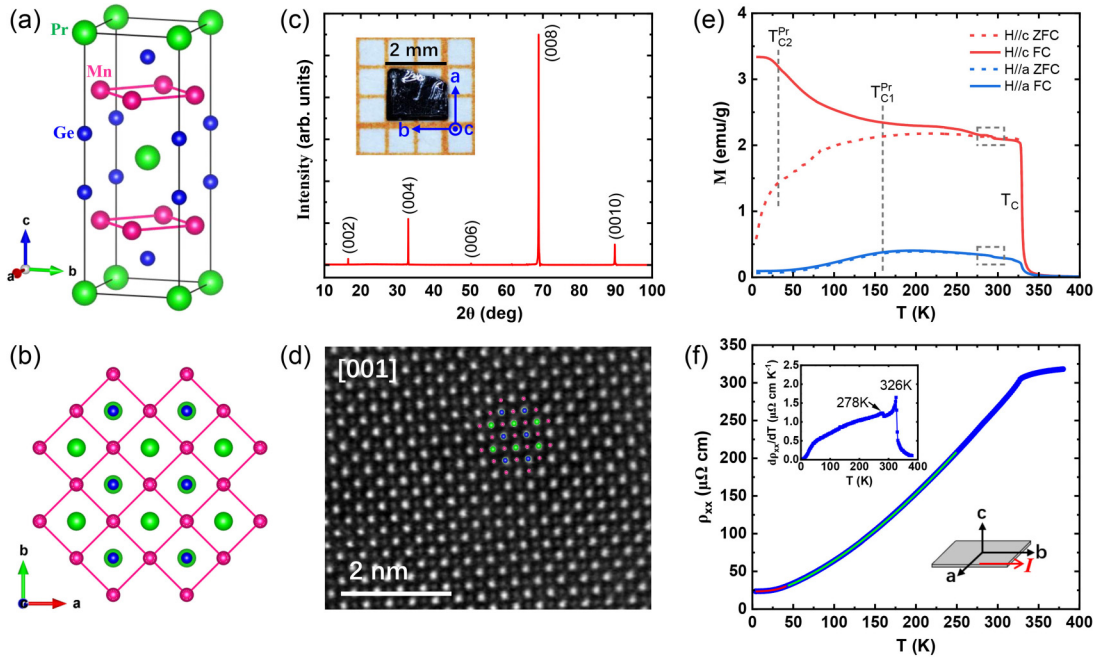

FIG. 1. (a), (b) Schematic diagram of crystal structures of $PrMn_2Ge_2$ viewed from the side and the top. (c) XRD pattern of the single crystal with the (00l) plane exposed in the surface. The inset shows a photograph of a typical $PrMn_2Ge_2$ crystal. (d) High-resolution lattice image taken from the [001] axis using STEM. (e) The temperature dependences of magnetization under zero field cooling (ZFC) and field cooling (FC) along $H//c$ and $H//a$ at 0.01 T. (e) Temperature dependence of in-plane, zero-field resistivity. Top inset: Derivative of resistivity with respect to temperature. Bottom inset: Sketch of the electric current relative to the crystallographic orientations.

typical metallic behavior. The derivative of resistivity, shown in the inset of Fig. 1(f), indicates two transitions at 326 and 278 K, corresponding to the ferromagnetic transitions and the canted to conical ferromagnetic transitions, respectively. The temperature dependence of resistivity measured below the conical ferromagnetic ordering temperature is divided into two regions and fitted using different laws. As shown in Fig. 1(f), the resistivity in a lower-temperature region can be well fitted using the formula of $\rho_{xx} = \rho_{xx0} + AT^2 + BT^{9/2}$ with $\rho_{xx0} = 23.41\,\mu\Omega\,\mathrm{cm}$, $A = 2.48 \times 10^{-3}\,\mu\Omega\,\mathrm{cm/K^2}$, and $B = 1.49 \times 10^{-7}\,\mu\Omega\,\mathrm{cm/K^{9/2}}$, where the AT^2 and $BT^{9/2}$ terms of the resistivity describe electron-magnon scattering and two-magnon scattering, respectively [26,27]. The B value is very small, suggesting the dominant contribution of electron-magnon scattering for the low-temperature resistivity. The resistivity in a higher-temperature region, i.e., intermediate temperate from 250 to about 40 K, can be well fitted using the formula of $\rho_{xx} = \rho_{xx0} + CT^{5/3}$, with $C = 2.04 \times 10^{-2}\,\mu\Omega\,\mathrm{cm/K^{5/3}}$, where the $CT^{5/3}$ describes the temperature dependence of the resistivity of spin fluctuation magnets [28].

Figures 2(a) and 2(b) show the anisotropic isothermal magnetization (M) versus applied field ($\mu_0 H$) for the $H//a$ axis and the $H//c$ axis at different temperatures, respectively. The magnetization reaches saturation more rapidly with the increasing field for $H//c$ than $H//a$, indicating that the easy magnetization axis of $PrMn_2Ge_2$ is along the c axis. The saturated magnetic moment increases with the decreasing temperature for $H//c$, as shown in Fig. 2(a). In contrast, the isothermal curves for the $H//a$ axis show completely different magnetization behavior at low temperatures, as shown in Fig. 2(b). The magnetization increases as temperature decreases down to 80 K and then it decreases. It is noted that the magnetization curves at 80 and 100 K show a nonlinear field dependence before the saturation, which is expected for a typically conical spin structure in $PrMn_2Ge_2$ [29]. Figures 2(c) and 2(d) show the temperature dependence of magnetization at given fields with $H//c$ and $H//a$. The data of the thermomagnetic curves were extracted from the isothermal magnetization in Figs. 2(a) and 2(b). It is consistent with direct measurements except for the constant magnetization for the low field with $H//c$ that is probably related to the domain wall pinning during the periodic high-field magnetization. It is worth noting that the magnetization for $H//a$ reaches the maximum at T^* with the decrease of temperature, and then decreases rapidly. Here T^* is the critical temperature corresponding to the maximum magnetization in different magnetic fields. The magnetization of the $H//a$ at $T < T^*$ rapidly decreases which is related to the magnetocrystalline anisotropy.

The magnetocrystalline anisotropy constants of $PrMn_2Ge_2$ were estimated by the approximation of $K_u = H_K M_S/2$ [30], where M_S is the saturation magnetization and H_K is the anisotropy field defined as the critical field above which the magnetization between the two magnetic field directions ($H//c$ and $H//a$) becomes consistent (see Fig. S2 [25]). The arrangements of the magnetic moment of Mn and Pr in different temperature regions are shown in the inset of Fig. 2(d). Above 300 K, the magnetocrystalline anisotropy constants caused by the canted ferromagnetic structure of Mn atoms are close to zero. The Mn atoms have a conical ferromagnetic configuration but the Pr atoms are not magnetically ordered in the temperature region of 290-160 K. Thus, the magnetocrystalline anisotropy changes little with decreasing temperature. At about 160 K, the magnetic ordering of Pr emerges and

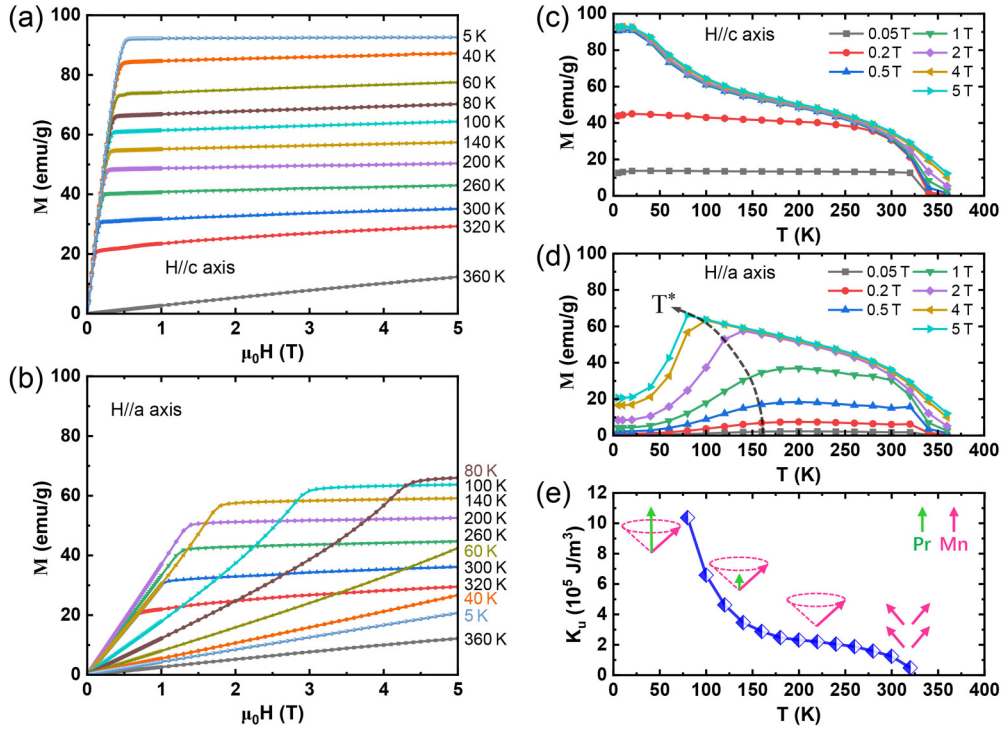

FIG. 2. The isothermal magnetization $M(\mu_0 H)$ curves at different temperatures for (a) $H//c$ axis and (b) $H//a$ axis. Temperature dependence of magnetization for (c) $H//c$ axis and (d) $H//a$ axis with the data taken from the $M(\mu_0 H)$ curves. (e) The temperature dependence of anisotropy constant (K_u). The insets show the schematic of the spin configurations at different temperature regions.

the magnetocrystalline anisotropy constant increases abruptly due to the strong single-ion anisotropy of the rare earth Pr [13,14]. Unlike the negligible temperature dependence of the magnetic moment of Mn, the magnetic moment of Pr along the c axis increases with decreasing temperature [12]. Thus, it is hard for the magnetic moments to be oriented along the external magnetic field with the $H//a$ axis because of the single-ion anisotropy of Pr with a nonzero orbital moment and the $4f$-$3d$ electrons' interaction [15] between Pr and Mn atoms. Therefore, the magnetic anisotropy can account for the decreasing trend of magnetization at $T < T^*$ in Fig. 2(d).

Figures 3(a) and 3(b) show the MR of $PrMn_2Ge_2$ at various temperatures in a magnetic field applied out of plane along the c axis and in the ab plane along the a axis. The MR decreases linearly with increasing magnetic field in the range of 300−40 K with the $H//c$ axis. The linear negative MR originates from the suppression of electron-magnon scattering on the application of a magnetic field [31]. A plateaulike MR appears at the low field below 60 K (see the details in Fig. S3 [25]) due to the competition between Pr and Mn magnetic moments [32]. Below 20 K, MR shows a nonlinear reduction due to the compensation of the positive MR generated by Lorentz forces to the linear negative MR [33]. For the $H//a$ axis, the MR shows a nonlinear increase before magnetization saturation, following a parabolic relationship. As shown in the schematic diagram in Fig. 3(c), when the magnetic field is applied along the a axis in the plane, the Mn moment tends to form a frustrationlike magnetic structure when the moment turns and is slowly aligned to the direction of the magnetic field, thus forming a nonlinear positive MR. When the magnetic moment is aligned completely along the external magnetic field, MR decreases linearly. Below 140 K, the opening of the parabola enlarges and the saturation field becomes higher. At low temperatures, the increase of the magnetic moment of Pr results in a strong magnetic anisotropy, and thus it is difficult for the magnetic moment to rotate toward the external field. The field dependence of MR is in agreement with the M-$\mu_0 H$ curves in Fig. 2. The MR for $H//a$ and $H//b$ in plane with $I//b$ were also measured (see Fig. S4 [25]). The measurements show that MR is almost isotropic in the ab plane. Figure 3(d) shows the temperature dependence of MR for the $H//a$ and $H//c$ directions under a magnetic field of 5 T. For the $H//c$, negative MR is maintained because the magnetization is fully saturated at 5 T magnetic field. In contrast, MR changes from negative to positive around 160 K as the temperature decreases for $H//a$. This positive MR at 5 T is attributed to the nonsaturating MR due to the emergence of the magnetic moment of Pr. As temperature decreases, the absolute value of MR decreases for $H//c$ and $H//a$. The decrease for $H//c$ can be attributed to a weakening of the negative MR by the Lorentz force at low temperatures [33], whereas the decrease for $H//a$ can be attributed to the unsaturated magnetic moment because of the increased magnetic anisotropy. The out-of-plane anisotropic magnetoresistance (AMR) ratio is defined as $MR_{//} - MR_{\perp}$ originating from the difference of in-plane and out of plane spin scatterings [33,34]. During cooling, AMR increases slowly in the temperature range from 300 to 160 K. However, it increases rapidly with decreasing temperature below 160 K and attains a maximum of 5.4% at 60 K. The trend of the temperature dependence of MR is consistent with that of the anisotropy constants in Fig. 2(e). At temperatures below 60 K, MR decreases

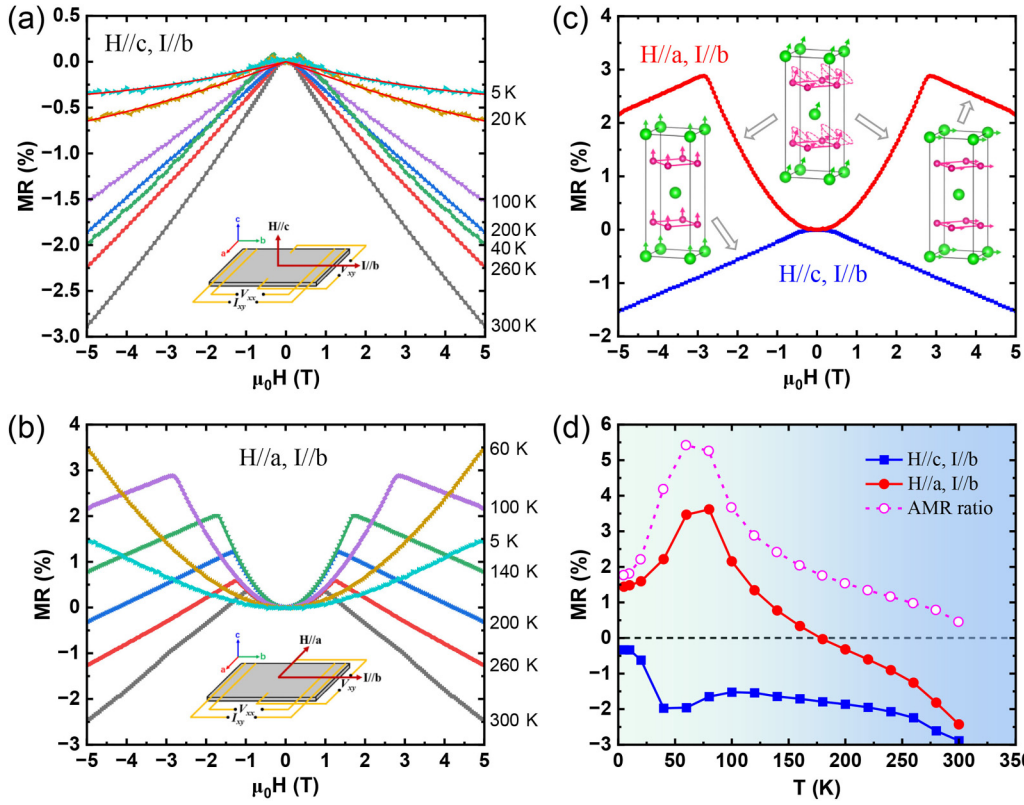

FIG. 3. Magnetoresistance with the magnetic field (a) out of the *ab* plane, *H*//*c*, and magnetic field (b) in the *ab* plane, *H*//*a*, and current along the *b* axis, *I*//*b*. The insets of (a), (b) show a schematic setup for measurements of resistivity and Hall resistivity when the magnetic field is out of plane and in plane, respectively. (c) Magnetoresistance at 100 K. The inset of (c) shows spin configurations corresponding to different magnetoresistance states. (d) Temperature dependence of MR and AMR ratio at $\mu_0 H = 5$ T.

for magnetic fields *H*//*a* and *H*//*c*, resulting in a decrease in the AMR ratio. Therefore, the magnetic ordering of Pr significantly enhances the anisotropy of the out of plane and in-plane MR.

Figure 4(a) presents the magnetic-field dependence of the Hall resistivity $\rho_{xy}(B)$ at different temperatures with *H*//*c*. Here ρ_{xy} was refined to allow for the demagnetization effect from the geometry of the parallelepiped sample, and $B = \mu_0[H + (1 - N_d)M]$, where the demagnetization factor $N_d = 0.68$ was calculated following a standard method [35]. With increasing magnetic fields, ρ_{xy} first increases rapidly and reaches a maximum, corresponding well to the saturated magnetic fields as shown in Fig. 2(a). Then it almost levels off with further increase of the magnetic fields. These results demonstrate that the AHE exists in $PrMn_2Ge_2$. It is known that the Hall resistivity ρ_{xy} in ferromagnets arises from two parts, $\rho_{xy} = \rho_{xy}^O + \rho_{xy}^A = R_0 B + R_S \mu_0 M$, where ρ_{xy}^O is the ordinary Hall resistivity due to the Lorentz force, ρ_{xy}^A is the anomalous Hall resistivity, R_0 is the ordinary Hall coefficient, and R_S is the anomalous Hall coefficient [8]. We can obtain the value of R_0 and ρ_{xy}^A from the linear fit of ρ_{xy} curves at the saturation region. The slope and the intercept of the *y* axis correspond to R_0 and ρ_{xy}^A, respectively. The carrier concentration (n) can be calculated from $R_0 = 1/ne$ [36], while the sign of R_0 determines the type of charge carriers. As shown in Fig. 4(b), the values of R_0 are all positive, confirming that the hole-type carriers are dominant. The carrier concentration increases abruptly below 300 K due to the possible change in the density of states at the Fermi surface induced by the canted to conical FM transition [37]. The carrier concentration shows a broad valley around 80 K. The valley means that a certain number of magnetic moments of Pr are ordered introducing a competition of long-range Ruderman-Kittel-Kasuya-Yosida (RKKY) and short-range exchange magnetic interactions [18] and bring about a change of the transport properties such as the Hall resistivity.

To understand the origin of the AHE in $PrMn_2Ge_2$, we have checked the scaling behavior of ρ_{xy}^A using the relation $\rho_{xy}^A = \beta \rho_{xx}^\alpha$ [38]. The dependency of $\log(\rho_{xy}^A)$ and $\log(\rho_{xx})$ is shown in Fig. 4(c). A scaling law parameter of $\alpha = 1.74$ is obtained and it confirms that the AHE originates from a combination of extrinsic and intrinsic mechanisms. To further ascertain the mechanism of the AHE, the dominant types of intrinsic and extrinsic contributions of the AHE resistivity are separated using the Tian-Ye-Jin scaling relation $\rho_{xy}^A = \alpha \rho_{xx0} + \beta \rho_{xx0}^2 + \gamma \rho_{xx}^2$, where ρ_{xx0} is the residual resistivity. α, β, and γ are the resistivity coefficients [9]. In this relation, the first two items on the right side of the equation represent extrinsic contributions related to the scattering affected by the spin-orbit interaction, i.e., the skew scattering and side-jump mechanisms [8,39]. The other is the intrinsic Kaplus-Luttinger (KL) contribution related to Berry curvature of electronic bands and

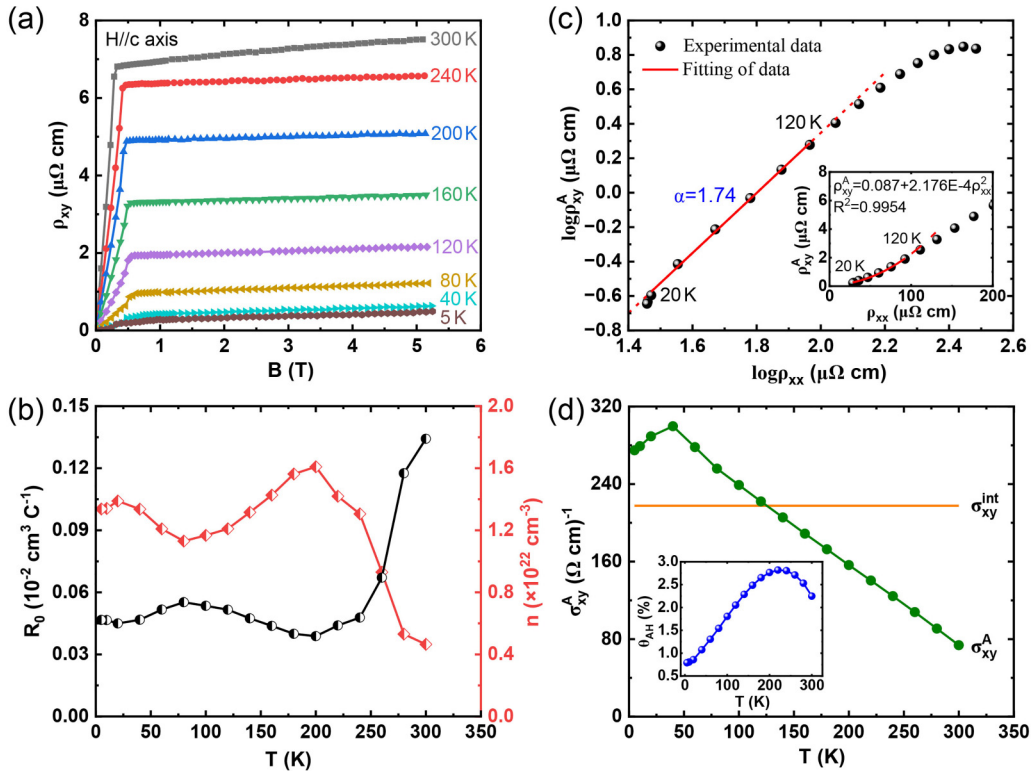

FIG. 4. (a) Anomalous Hall resistivity with the external magnetic field applied along the c axis. (b) Temperature dependence of the ordinary Hall coefficient and the carrier concentration. (c) The plot of log (ρ_{xy}^A) versus log (ρ_{xx}). The inset of (c) shows the plot of ρ_{xy}^A versus ρ_{xx}. (d) Temperature dependence of the anomalous Hall conductivity. The inset of (d) shows the temperature dependence of the anomalous Hall angle.

varies with ρ_{xx}^2 [40]. The inset of Fig. 4(c) shows the scaling behavior of ρ_{xy}^A versus ρ_{xx}. Thus, the intrinsic anomalous Hall conductivity (AHC) ($\sigma_{xy,\text{in}}^A \approx \frac{\gamma\rho_{xx}^2}{\rho_{xx}^2}$) of 217.6 Ω^{-1} cm^{-1} for the $PrMn_2Ge_2$ compound can be obtained from the fitting. As shown in Fig. 4(d), $\sigma_{xy,\text{in}}^A$ reaches ~79% of the total Hall conductivity, being the dominant contribution to the observed AHE at 5 K. The intrinsic anomalous Hall conductivity is similar to the maximum value in other rare earth intermetallic compounds, such as $CeMn_2Ge_2$ ($\sigma_{xy,\text{in}}^A \sim 276\,\Omega^{-1}\,\text{cm}^{-1}$) [7] and $GdMn_6Sn_6$ ($\sigma_{xy,\text{in}}^A \sim 223\,\Omega^{-1}\,\text{cm}^{-1}$) [41].

Figure 4(d) shows the temperature dependence of the total AHC ($\sigma_{xy}^A \approx \frac{\rho_{xy}^A}{\rho_{xx}^2}$) for $PrMn_2Ge_2$. The AHC increases monotonically with decreasing temperature and a maximum of about 300 Ω^{-1} cm^{-1} is attained at 40 K. It should be noted that σ_{xy}^A deviates from a linear relation below 40 K, which is probably related to the enhanced electron-magnon scattering due to the perfect ordering of Pr at low temperatures. Theoretically, the intrinsic contribution of $|\sigma_{xy,\text{in}}^A|$ is of the order of $e^2/(hc)$, where e is the electronic charge, h is the Planck constant, and c is the lattice constant. Taking $c = 10.929$ Å [42], $|\sigma_{xy,\text{in}}^A|$ is ~ 355 Ω^{-1} cm^{-1}. Therefore, the intrinsic AHC derived from the Tian-Ye-Jin scaling relation is ~0.61 $e^2/(hc)$. By contrast, the extrinsic side-jump contribution of $|\sigma_{xy,\text{sj}}^A|$ is of the order of $e^2/(hc)(\varepsilon_{\text{SO}}/E_{\text{F}})$, where ε_{SO} and E_{F} are the spin-orbit interaction (SOI) and Fermi energy, respectively [43,44]. Since the $\varepsilon_{\text{SO}}/E_{\text{F}}$ is usually less than 0.01 for metallic ferromagnets, thus the extrinsic side-jump contribution should be very small compared to the intrinsic Berry phase KL contribution. The anomalous Hall angle ($\theta = \sigma_{xy}^A/\sigma_{xx}$) is shown in the inset of Fig. 4(d). The maximum anomalous Hall angle of $PrMn_2Ge_2$ is determined to be 2.8%, which is comparable to that of most intermetallic compounds [23,45]. Moreover, the value of θ is not constant with temperature, indicating that the AHE of $PrMn_2Ge_2$ is not dominated by the extrinsic skew scattering.

A second approach based on the relation between anomalous Hall conductivity σ_{xy}^A and saturation magnetization M_{S} was used to determine the dominant contributions to the AHE in this compound. Figure 5(a) shows the temperature dependence of σ_{xy}^A and M_{S}. For the intrinsic AHE dominated by the Kaplus-Luttinger (KL) theory, the anomalous Hall conductivity σ_{xy}^A is linearly proportional to Ms [46,47]. As shown in Fig. 5(a), σ_{xy}^A exhibits two-stage linear dependence of M_{S} due to the ordering of the magnetic moment of Pr atoms. Thus, the scaling factor $S_{\text{H}} = \mu_0 R_{\text{S}}/\rho_{xx}^2 = \sigma_{xy}^A/M_{\text{S}}$ should be constant and temperature independent. S_{H} in high-temperature and low-temperature regions was determined from the slope of the two linear relations between σ_{xy}^A and M_{S} to be $S_1 = 0.19\,\text{V}^{-1}$ and $S_2 = 0.08\,\text{V}^{-1}$, respectively. These values are comparable to those found in traditional itinerant ferromagnets such as Fe and Ni ($S_{\text{H}} \sim 0.01$–$0.2\,\text{V}^{-1}$) [48,49]. Figure 5(b) shows the scaling plots of the modified anomalous Hall resistivity $\rho_{xy}^A/\mu_0 B$ and resistivity $\rho_{xx}^2 M/\mu_0 B$ over the whole temperature range. A fairly linear temperature dependence is observed confirming that the AHE in $PrMn_2Ge_2$ is dominated by the intrinsic KL mechanism.

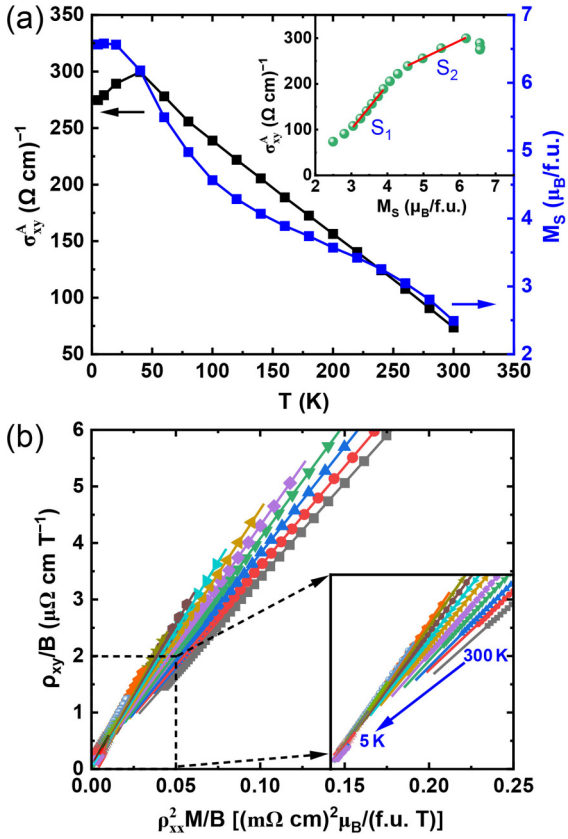

FIG. 5. (a) Temperature dependence of σ^A_{xy} and M_S. The inset shows σ^A_{xy} versus saturated magnetization (M_S). (b) The ρ^A_{xy}/B versus $\rho^2_{xx}M/\mu_0 B$ curves from 300 to 5 K with a temperature step of 20 K.

Figure 6(a) shows the field dependence of the Hall resistivity for the in-plane magnetic field of the $H//a$ axis at different temperatures. The transverse Hall resistivity ρ_{xy} shows a cusp when the temperature is above 80 K. The cusps gradually weakened and their corresponding magnetic field increased with decreasing temperature. The anomalous planar Hall resistivity here resembles a topological signal, known as the planar topological Hall effect (PTHE) [19,22]. The conical magnetic configuration of $PrMn_2Ge_2$ has magnetic moments which are believed to have a component parallel to the external magnetic field and a transverse component akin to the conventional helical structure. Therefore, conical magnets naturally promote the PTHE, as theoretically predicted [19]. A recent study of magnetic domain structure by Hou *et al.* has revealed that the $PrMn_2Ge_2$ can host skyrmionic bubbles in a wide temperature range [3]. Thus, the PTHE here could be intrinsic and originates from the real-space skyrmionic bubbles rather than being related to the in-plane AMR. To further confirm our argument, the angular-dependent in-plane AMR and PHE of the $PrMn_2Ge_2$ were measured simultaneously at a ferromagnetic state of 300 K in a saturation field of 3 T (see Fig. S5 [25]). The AMR of $PrMn_2Ge_2$ shows a maximum of 0.02% at 3 T, which is negligible compared to the AMR for conventional transition metal compounds [34,50]. The PHE characterized by the transverse Hall resistivity can be well fitted following the work of Li *et al.* [51], and then the in-plane AMR and intrinsic PHE contribution can be separated. As shown in Fig. S5 [25], the analysis shows that the in-plane AMR effect is quite small, and thus the PTHE in $PrMn_2Ge_2$ is due to the in-plane topological spin texture related to the real-space skyrmionic bubbles. The skyrmionic bubbles act as a fictitious magnetic field that finally results in the appearance of the cusp that resembles the topological Hall effect. The field-dependent anomalous planar Hall variables have very recently been observed in several skyrmion-hosting materials such as Fe_3Sn_2 [22], Cr_5Te_8 [23], and Fe_3GeTe_2 [24,52]. It is generally attributed to a nonzero spin chirality by a noncoplanar spin texture, that acts as an effective gauge field for the origin of an exotic planar Hall-like signal. Thus, we can also attribute the PTHE of $PrMn_2Ge_2$ to a similar mechanism. As shown in Fig. 6(b), the conical magnetic structure of Mn turns toward a magnetic field applied along the a axis such

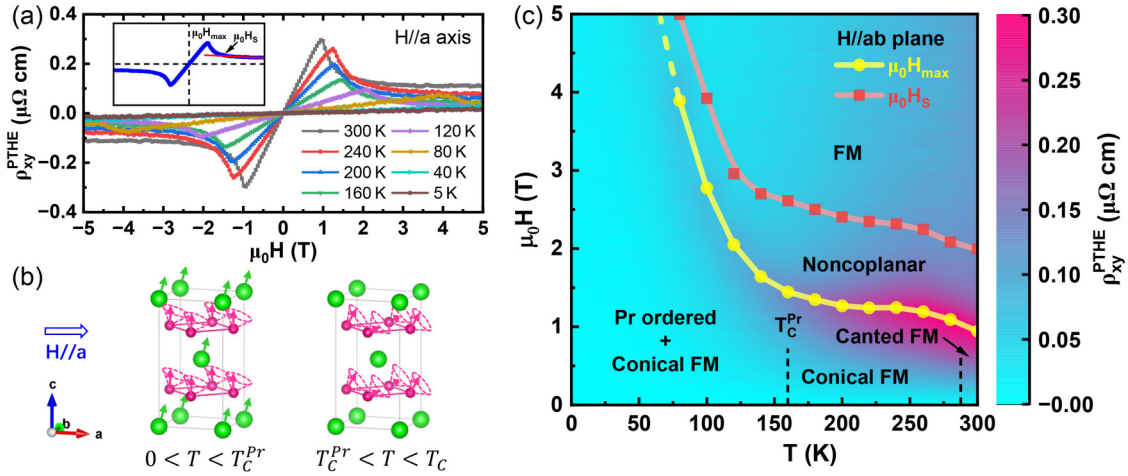

FIG. 6. (a) Planar topological Hall resistivity with the $H//a$ axis. (b) Magnetic phase diagram of the $PrMn_2Ge_2$ single crystal. The yellow and red solid circles correspond to the critical field for the maximum values ($\mu_0 H_{max}$) and the vanishing ($\mu_0 H_S$) of the planar topological Hall resistivities, respectively. (c) The schematic spin configurations of Mn and Pr moments at $0 < T < T_C^{Pr}$ and $T_C^{Pr} < T < T_C$. The inset of (a) shows the schematic diagram for defining the $\mu_0 H_{max}$ and $\mu_0 H_S$.

that a noncoplanar spin configuration appears. This noncoplanar spin configuration leads to spin chirality in the conical magnetic structure of the Mn atoms. It causes a real-space nonvanishing Berry curvature, which acts as a fictitious magnetic field and produces an additional Hall signal, namely, the PTHE. The PTHE disappears at a high magnetic field because a stable collinear ferromagnetic structure is formed. Below 80 K, the PTHE was not observed because the applied in-plane magnetic field was not large enough to overcome the enhanced magnetocrystalline anisotropy.

Based on the observation of the magnetoelectric transport properties, we propose a magnetic phase diagram for the $PrMn_2Ge_2$ compound [Fig. 6(c)]. In the low magnetic field region, the magnetic phase diagram is divided into three regions: canted ferromagnetic, conical ferromagnetic, and coexistence of Pr ordered and conical ferromagnetic. In these regions, a noncoplanar magnetic structure is formed upon the application of an in-plane magnetic field. The magnetic phase diagram plots the magnetic field ($\mu_0 H_{\max}$) corresponding to the maximum value of PTHE and the critical magnetic field ($\mu_0 H_S$) where PTHE disappears. The $\mu_0 H_{\max}$ and $\mu_0 H_S$ are defined as shown in the inset of Fig. 6(a). It should be emphasized that the critical magnetic field of PTHE increases rapidly with decreasing temperature after the ordering of the Pr magnetic moment. Figure 6(b) shows the magnetic structure of $PrMn_2Ge_2$ and the left and right panels correspond to the case with and without ordering of magnetic moments of Pr atoms, respectively. At temperatures above T_{C1}^{Pr}, only Mn atoms carry a magnetic moment and form a conical magnetic structure. The spin chirality of the noncoplanar conical magnetic moment of the Mn atoms is induced upon rotating to the external field. Once the ferromagnetic ordering of Pr is established, it is rather difficult to rotate the conically arranged magnetic moment of Mn atoms to the direction of the external field because of the strong single-ion anisotropy of Pr and $4f$-$3d$ interaction [13–15], and thus a higher critical magnetic field is required to generate a PTHE. Theoretically, the critical magnetic field for the occurrence of PTHE for $PrMn_2Ge_2$ and its size can be adjusted by doping with other rare earth ions of different anisotropy. This possibility will be explored in the future.

IV. CONCLUSION

We have grown high-quality $PrMn_2Ge_2$ single crystals using the flux method and systematically investigated the anisotropy of the magnetoelectronic transport properties of this ternary compound by applying a magnetic field along the primary crystallographic axes. A significant magnetocrystalline anisotropy has been revealed. For $H//c$ and $I//b$, the compound exhibits a linear MR and a conventional AHE. Analysis of the magnetotransport data using the Tian-Ye-Jin scaling relation and the linear relationship between $\rho_{xy}^A/\mu_0 H$ and $\rho_{xx}^2 M/\mu_0 H$ indicate that the AHE of $PrMn_2Ge_2$ is dominated by the intrinsic Berry curvature mechanism. A nonlinear positive MR and a large PTHE have been observed with $H//a$ and $I//b$ and they both arise from the field-induced noncoplanar spin textures with nonzero spin chirality. The emergence of the ferromagnetic ordering of the Pr atoms at low temperatures strongly enhances the magnetocrystalline anisotropy and it increases the saturation magnetic field of nonlinear MR and the critical field for the maximum values of PTHE. It has been suggested that the magnitude and the critical field for the MR and PTHE can be manipulated by the magnetic ordering of the rare earth atoms, indicating that the conical ferromagnetic $PrMn_2Ge_2$ single crystal is an excellent candidate for functional applications in spintronic devices.

Note added. A related work, Ref. [53], on the anisotropic magnetism and the anomalous Hall effect of $PrMn_2Ge_2$ single crystal was published after our submission. Except for the common magnetic anisotropy, we focus on the electrical transport properties of $PrMn_2Ge_2$ single crystals for the in-plane ($H//a$) and out-of-plane ($H//c$) directions, while Ref. [53] only reported that for the out of plane ($H//c$) direction. More importantly, we observed a planar topological Hall effect at the $H//a$ direction and showed a complete magnetic phase diagram.

ACKNOWLEDGMENTS

This work was financially supported by the National Key R&D Program of China (Grant No. 2022YFA1402600) and the National Natural Science Foundation of China (Grants No. 51831003 and No. 12274321).

[1] N. P. Kolmakova, A. A. Sidorenko, and R. Z. Levitin, Low Temp. Phys. **28**, 653 (2002).
[2] P. Kumar, K. G. Suresh, A. K. Nigam, A. Magnus, A. A. Coelho, and S. Gama, Phys. Rev. B **77**, 224427 (2008).
[3] Z. Hou, L. Li, C. Liu, X. Gao, Z. Ma, G. Zhou, Y. Peng, M. Yan, X. Zhang, and J. Liu, Mater. Today Phys. **17**, 100341 (2021).
[4] S. Wang, Q. Zeng, D. Liu, H. Zhang, L. Ma, G. Xu, Y. Liang, Z. Zhang, H. Wu, R. Che *et al.*, ACS Appl. Mater. Interfaces **12**, 24125 (2020).
[5] Z. Hou, W. Ren, B. Ding, G. Xu, Y. Wang, B. Yang, Q. Zhang, Y. Zhang, E. Liu, F. Xu *et al.*, Adv. Mater. **29**, 1701144 (2017).
[6] G. Gong, L. Xu, Y. Bai, Y. Wang, S. Yuan, Y. Liu, and Z. Tian, Phys. Rev. Mater. **5**, 034405 (2021).
[7] L. Xu, Y. Bai, G. Gong, F. Song, Z. Li, Y. Han, L. Ling, and Z. Tian, Phys. Rev. B **105**, 075108 (2022).
[8] N. Nagaosa, J. Sinova, S. Onoda, A. H. MacDonald, and N. P. Ong, Rev. Mod. Phys. **82**, 1539 (2010).
[9] Y. Tian, L. Ye, and X. Jin, Phys. Rev. Lett. **103**, 087206 (2009).
[10] P. Bruno, V. K. Dugaev, and M. Taillefumier, Phys. Rev. Lett. **93**, 096806 (2004).
[11] A. Neubauer, C. Pfleiderer, B. Binz, A. Rosch, R. Ritz, P. G. Niklowitz, and P. Boni, Phys. Rev. Lett. **102**, 186602 (2009).
[12] R. Welter, G. Venturini, E. Ressouche, and B. Malaman, J. Alloys Compd. **218**, 204 (1995).
[13] A. Ermolenko, IEEE Trans. Magn. **12**, 992 (1976).
[14] J. J. M. Franse, F. E. Kayzel, and N. P. Thuy, J. Magn. Magn. Mater. **129**, 26 (1994).
[15] D. Givord, C. Lacroix, and D. Schmitt, Curr. Opin. Solid State Mater. Sci. **1**, 183 (1996).

[16] J. L. Wang, L. Caron, S. J. Campbell, S. J. Kennedy, M. Hofmann, Z. X. Cheng, M. F. Md Din, A. J. Studer, E. Brück, and S. X. Dou, Phys. Rev. Lett. **110**, 217211 (2013).

[17] K. S. V. L. Narasimhan, V. U. S. Rao, R. L. Bergner, and W. E. Wallace, J. Appl. Phys. **46**, 4957 (1975).

[18] M. Song, J. Zhao, C. Liu, M. He, Y. Wang, Y. Han, L. Ling, L. Cao, L. Zhang, Z. Qu *et al.*, Appl. Phys. Lett. **120**, 092402 (2022).

[19] N. Mohanta, S. Okamoto, and E. Dagotto, Phys. Rev. B **102**, 064430 (2020).

[20] H. X. Tang, R. K. Kawakami, D. D. Awschalom, and M. L. Roukes, Phys. Rev. Lett. **90**, 107201 (2003).

[21] A. A. Burkov, Phys. Rev. B **96**, 041110(R) (2017).

[22] H. Li, B. Ding, J. Chen, Z. Li, X. Xi, G. Wu, and W. Wang, Appl. Phys. Lett. **118**, 182407 (2021).

[23] Y. Wang, J. Yan, J. Li, S. Wang, M. Song, J. Song, Z. Li, K. Chen, Y. Qin, L. Ling, H. Du, L. Cao, X. Luo, Y. Xiong, and Y. Sun, Phys. Rev. B **100**, 024434 (2019).

[24] Y. You, Y. Gong, H. Li, Z. Li, M. Zhu, J. Tang, E. Liu, Y. Yao, G. Xu, F. Xu, and W. Wang, Phys. Rev. B **100**, 134441 (2019).

[25] See Supplemental Material at http://link.aps.org/supplemental/10.1103/PhysRevB.107.224417 for the energy-dispersive spectroscopy analysis (Fig. S1), calculation method of anisotropy constant (Fig. S2), magnetoresistance for $H//c$ out of plane and $H//a$ in plane with $I//b$ at various temperatures (Fig. S3), magnetoresistance for $H//a$ and $H//b$ in plane with $I//b$ at various temperatures for $PrMn_2Ge_2$ (Fig. S4), and angular-dependent in-plane AMR and PHE (Fig. S5).

[26] D. Rani, J. Kangsabanik, K. G. Suresh, N. Patra, D. Bhattacharyya, S. N. Jha, and A. Alam, Phys. Rev. Appl. **10**, 054022 (2018).

[27] K. Kubo and N. Ohata, J. Phys. Soc. Jpn. **33**, 21 (1972).

[28] S. Gardelis, J. Androulakis, P. Migiakis, J. Giapintzakis, S. K. Clowes, Y. Bugoslavsky, W. R. Branford, Y. Miyoshi, and L. F. Cohen, J. Appl. Phys. **95**, 8063 (2004).

[29] J. Kishine and A. S.Ovchinnikov, Solid State Phys. **66**, 1 (2015).

[30] M. T. Johnson, P. J. H. Bloemen, F. J. A. d. Broeder, and J. J. d. Vries, Rep. Prog. Phys. **59**, 1409 (1996).

[31] B. Raquet, M. Viret, E. Sondergard, O. Cespedes, and R. Mamy, Phys. Rev. B **66**, 024433 (2002).

[32] D. Huang, H. Li, B. Ding, X. Xi, J. Gao, Y.-C. Lau, and W. Wang, Appl. Phys. Lett. **121**, 232404 (2022).

[33] N. Kumar, Y. Soh, Y. Wang, and Y. Xiong, Phys. Rev. B **100**, 214420 (2019).

[34] T. McGuire and R. Potter, IEEE Trans. Magn. **11**, 1018 (1975).

[35] A. Aharoni, J. Appl. Phys. **83**, 3432 (1998).

[36] Q. Wang, S. Sun, X. Zhang, F. Pang, and H. Lei, Phys. Rev. B **94**, 075135 (2016).

[37] J. H. V. J. Brabers, K. H. J. Buschow, and F. R. de Boer, Phys. Rev. B **59**, 9314 (1999).

[38] S. Roy, R. Singha, A. Ghosh, A. Pariari, and P. Mandal, Phys. Rev. B **102**, 085147 (2020).

[39] L. Berger, Phys. Rev. B **2**, 4559 (1970).

[40] R. Karplus and J. M. Luttinger, Phys. Rev. **95**, 1154 (1954).

[41] T. Asaba, S. M. Thomas, M. Curtis, J. D. Thompson, E. D. Bauer, and F. Ronning, Phys. Rev. B **101**, 174415 (2020).

[42] D. Rossi, R. Marazza, D. Mazzone, and R. Ferro, J. Less-Common Met. **59**, 79 (1978).

[43] P. Nozières and C. Lewiner, J. Phys. **34**, 901 (1973).

[44] S. Onoda, N. Sugimoto, and N. Nagaosa, Phys. Rev. Lett. **97**, 126602 (2006).

[45] E. Liu, Y. Sun, N. Kumar, L. Muechler, A. Sun, L. Jiao, S. Yang, D. Liu, A. Liang, Q. Xu *et al.*, Nat. Phys. **14**, 1125 (2018).

[46] C. Zeng, Y. Yao, Q. Niu, and H. H. Weitering, Phys. Rev. Lett. **96**, 037204 (2006).

[47] S. Friedemann, M. Brando, W. J. Duncan, A. Neubauer, C. Pfleiderer, and F. M. Grosche, Phys. Rev. B **87**, 024410 (2013).

[48] N. V. Volkenshtein and G. V. Fedorov, J. Exp. Theor. Phys **11**, 48 (1960).

[49] S. N. Kaul, Phys. Rev. B **20**, 5122 (1979).

[50] A. W. Rushforth, K. Výborný, C. S. King, K. W. Edmonds, R. P. Campion, C. T. Foxon, J. Wunderlich, A. C. Irvine, P. Vašek, V. Novák, K. Olejník, J. Sinova, T. Jungwirth, and B. L. Gallagher, Phys. Rev. Lett. **99**, 147207 (2007).

[51] P. Li, C. H. Zhang, J. W. Zhang, Y. Wen, and X. X. Zhang, Phys. Rev. B **98**, 121108(R) (2018).

[52] J. Macy, D. Ratkovski, P. P. Balakrishnan, M. Strungaru, Y. C. Chiu, A. Flessa Savvidou, A. Moon, W. Zheng, A. Weiland, G. T. McCandless *et al.*, Appl. Phys. Rev. **8**, 041401 (2021).

[53] X. Y. Wang, S. Xu, H. Wang, J. F. Lin, X. Y. Zeng, X. P. Ma, J. Gong, Y. T. Wang, K. Han, and T. L. Xia, Phys. Rev. B **107**, 144402 (2023).